Elsevier Editorial System(tm) for Journal Of Computational Physics
Manuscript Draft

Manuscript Number:

Title: Anti-diffusion method for interface steepening in two-phase incompressible flow

Article Type: Regular Article

Keywords: two-phase flow; volume-of-fluid; interface steepening; anti-diffusion; unstructured meshes

Corresponding Author: Mr. Kwok Kai So,

Corresponding Author's Institution: Technical University Munich

First Author: Kwok Kai So

Order of Authors: Kwok Kai So; Xiangyu Hu; Nikolaus A Adams

Abstract: In this paper, we present a method for obtaining sharp interfaces in two-phase incompressible flow by an anti-diffusion correction. The underlying discretization is based on the volume-of-fluid (VOF) interface-capturing method. The key idea is to steepen the interface by solving the diffusion equation with reverse time, i.e. an anti-diffusion equation, after each advection step of the volume fraction. As a solution of the anti-diffusion equation requires regularization, a limiter based on the directional derivative is developed for calculating the gradient of the volume fraction. This limiter ensures the boundedness of the volume fraction. The formulation of the limiter and the algorithm for solving the anti-diffusion equation are suitable for 3-dimensional unstructured meshes. Validation computations are performed for 2- and 3- dimensional rising-bubble and rising-drop configurations, and for Cartesian and non-Cartesian meshes. The results demonstrate that sharp interfaces can be recovered reliably and that the results agree with previous simulations based on different interface methods and with experiments.

Suggested Reviewers: William J. Rider
wjr@lanl.gov
Dr. Rider is one of the main contributors of VOF method which is the underlying method used in the present manuscript.

Marcus Herrmann
marcus.herrmann@asu.edu
Dr. Herrmann is an active researcher on the high-accuracy modeling of multi-phase flows which is the focus of the present manuscript.

Shingyu Leung
masyleung@ust.hk
Dr. Leung is also an active researcher in multi-phase flow modeling.

Anti-diffusion method for interface steepening in two-phase incompressible flow

K. K. So, X. Y. Hu and N. A. Adams

Lehrstuhl für Aerodynamik, Technische Universität München, 85748 Garching, Germany

Abstract

In this paper, we present a method for obtaining sharp interfaces in two-phase incompressible flow by an anti-diffusion correction. The underlying discretization is based on the volume-of-fluid (VOF) interface-capturing method. The key idea is to steepen the interface by solving the diffusion equation with reverse time, i.e. an anti-diffusion equation, after each advection step of the volume fraction. As a solution of the anti-diffusion equation requires regularization, a limiter based on the directional derivative is developed for calculating the gradient of the volume fraction. This limiter ensures the boundedness of the volume fraction. The formulation of the limiter and the algorithm for solving the anti-diffusion equation are suitable for 3-dimensional unstructured meshes. Validation computations are performed for 2- and 3- dimensional rising-bubble and rising-drop configurations, and for Cartesian and non-Cartesian meshes. The results demonstrate that sharp interfaces can be recovered reliably and that the results agree with previous simulations based on different interface methods and with experiments.

Key words: two-phase flow, volume-of-fluid, interface steepening, anti-diffusion, unstructured meshes

1. Introduction

The numerical simulation of two-phase incompressible flows is an area of high interest in academia and industry. Various approaches have been developed. Two main directions are interface-tracking methods and interface-capturing methods.

With interface-tracking methods, the location of the interface is explicitly represented. Examples of interface-tracking methods include front tracking methods [1, 2] and marker methods [3, 4]. These latter, e.g., can effectively locate the interface position by interface markers. However, they encounter difficulties for large interface deformations and topology changes, and require a special treatment of the interface marker distribution when the interface is stretched or compressed.

On the other hand, interface-capturing methods do not explicitly track the location of the interface, but capture the location of the interface implicitly. Examples of interface-capturing methods include the level-set method and the volume-of-fluid (VOF) method. With the level-set method the interface is defined as the zero contour of a signed-distance function - the level-set function. The interface is sharp by definition and sharpness is maintained by recovering the signed distance property of the level-set function through reinitialization. From the level-set function the curvature of the interface and the surface tension can be calculated with high accuracy. However, a main drawback of the level-set method is lack of discrete conservation. We refer to references [5] and [6] for a detailed description of the level-set method.

With VOF methods, the two phases are defined by the volume fraction which assumes values between 0 and 1. The interface is represented by the transition region where the volume fraction ramps up from 0 to 1. The main advantage of VOF methods is the exact conservation of mass. One main drawback of VOF methods is that the interface cannot be located precisely, which leads to inaccuracies in calculating interface curvature and thus surface tension. References [7] and [4] provide an overall review of VOF methods.

To obtain a sharp interface for VOF methods, two methodologies are generally used. First, with VOF volume-tracking methods, the interface is reconstructed before each advection step, and subsequently the flow is updated by propagating the reconstructed interface. Different interface-reconstruction schemes have been developed, the basic ones include simple line interface calculation (SLIC) [8], SOLA-VOF [9] and piecewise-linear interface construction (PLIC) [4]. For the interface-propagation step the operator split method is generally used [4]. Drawbacks of the VOF volume-tracking method are: the curvature of the reconstructed interface is not smooth, which leads to inaccuracies in the interface propagation step; the interface propagation can become unstable for very complex interfaces. Unphysical flows, termed "flotsam" and "jetsam", can be created due to the errors induced by the volume-tracking algorithm [7]. Second, instead of reconstructing and propagating the interface as with the VOF volume-tracking method, in VOF volume-capturing methods the volume fraction is advected with a special treatment to reduce the numerical diffusion. Examples include the introduction of an artificial-compression term in the advection equation [10].

For all methods, one prime criterion of accurate two-phase flow simulation is to maintain a sufficiently sharp interface throughout the simulation. How to obtain a sharp interface with interface-capturing methods has been studied by a number of researchers in the past. Examples include the usage of a compressive scheme which blends an upwind differencing scheme and a higher-order differencing scheme for the advection step [11], limited downwind anti-diffusive flux correction [12], and the use of artificial compression as an intermediate step [13]. In this paper, we propose a regularized anti-diffusion correction technique which can be used in a straight-forward fashion with underlying VOF discretization schemes on regular or irregular meshes. We demonstrate that by this correction technique, applied after the VOF advection step, a desired interface sharpness can be recovered reliably and efficiently.

For interface steepening methods it is possible to impose a parameter to define the desired interface thickness for obtaining convergence and stability, for example in [13, 14] the interface thickness is related to the grid size through a parameter d. However, determination of parameters defining the interface thickness is empirical. Alternatively, as is the case for our anti-diffusion-correction algorithm presented in this paper, a stopping criterion for the correction step can be developed. The stopping criterion should be normalized such that it is case- and grid-resolution-independent.

The governing equations and an overview of the solution procedure are presented in Section 2. The main focus of the paper, which is the formulation of the anti-diffusion equation and the solution algorithm, is presented in Section 3. Numerical cases and results are presented in Section 4. Finally, concluding remarks are given in Section 5.

2. Governing equations

In this paper, the open source CFD package, *OpenFOAM* [15] is employed as the simulation platform. This procedure underlines the fact that the proposed anti-diffusion correction can be used in a straight-forward fashion with any underlying VOF discretization scheme. *OpenFOAM* is a finite-volume package for solving partial differential equations on 3-dimensional unstructured meshes. The solver *interFoam* in the *OpenFOAM* package is designated for solving two-phase flow using a VOF volume-capturing method and is utilized as the basis for developing the anti-diffusion correction method in this paper. The main part of the solution procedure of the solver is described by Rusche [10]. The governing equations for unsteady, incompressible, viscous, immiscible two-phase flow are given by the continuity equation and the Navier-Stokes equation

$$\nabla \cdot \mathbf{u} = 0 \tag{1}$$

$$\frac{\partial \rho \mathbf{u}}{\partial t} + \nabla \cdot (\rho \mathbf{u}\mathbf{u}) = -\nabla p + \nabla \cdot \boldsymbol{T} + \rho \mathbf{g} + \mathbf{f}_\sigma \quad , \tag{2}$$

where $\mathbf{u}$ is the velocity, ρ is the density, t is the time, p is the pressure, $\boldsymbol{T}$ is the stress tensor, $\mathbf{g}$ is the gravitational acceleration, and $\mathbf{f}_\sigma$ is the force due to surface tension. For a two-phase flow, the two fluids are represented by the volume fraction α which is defined as

$$0 \leq \alpha \leq 1 \quad , \tag{3}$$

where $\alpha = 0$ refers to the first fluid, $\alpha = 1$ refers to the second fluid, and $0 < \alpha < 1$ refers to the transitional region, i.e. the interface between the two fluids. The volume fraction is advected by the flow, resulting in the volume-fraction-transport equation

$$\frac{\partial \alpha}{\partial t} + \nabla \cdot (\alpha \mathbf{u}) = 0 \quad . \tag{4}$$

The local density ρ and viscosity μ are given by

$$\rho = \alpha \rho_1 + (1 - \alpha)\rho_2 \tag{5}$$

$$\mu = \alpha \mu_1 + (1 - \alpha)\mu_2 \quad , \tag{6}$$

where the subscripts 1 and 2 denote the respective fluids of the two-phase flow. The stress tensor is given by Newton's law

$$\boldsymbol{T} = \mu(\nabla \mathbf{u} + \nabla \mathbf{u}^T) \quad . \tag{7}$$

The surface curvature of the interface κ is given by

$$\kappa = \nabla \cdot \left(\frac{\nabla \alpha}{|\nabla \alpha|} \right) \quad . \tag{8}$$

The force due to surface tension is formulated by the Continuum Surface Force (CSF) as given by Brackbill et al. [16]

$$\mathbf{f}_\sigma = -\sigma \kappa \nabla \alpha \quad , \tag{9}$$

where σ is the surface tension.

The above governing equations define the continuity of mass and momentum of the incompressible two-phase flow. For obtaining a sharp phase-interface, a new element of the solution algorithm - the anti-diffusion correction - is introduced and defined by

$$\frac{\partial \alpha}{\partial \tau} = \nabla \cdot (D \nabla \alpha) \quad , \tag{10}$$

where D is the diffusion coefficient and τ is a pseudo time for evolving the anti-diffusion correction. In the diffusion equation (10), positive D represents a normal diffusion process, while negative D represents a diffusion process with reverse time, which can be regarded as an anti-diffusion process.

The discretization of the advection equation and momentum equation follows the underlying *OpenFOAM* algorithm as given in [10]. First, the advection equation (4) is evaluated for one time step based on the TVD limiter by Jasak et al. [17]. Subsequently, the new part, the anti-diffusion-correction, equation (10) is solved after each time step of the advection equation (4). The density and viscosity updates are computed from the new volume-fraction field. Subsequently, the momentum and continuity equations are solved by the PISO algorithm by Issa [18], as available in *OpenFOAM*.

The main focus of this paper is the anti-diffusion correction after the advection step, and the rest of the paper is devoted to the detailed description of the anti-diffusion correction. For a comprehensive description of the other details of the solution procedure as provided by *OpenFOAM* the reader is referred to references [11, 10, 15, 17, 18, 19].

3. Anti-diffusion correction

3.1. Formulation of the 1-dimensional anti-diffusion equation

Before formulating the anti-diffusion correction for 3-dimensional flow simulations, the essential properties of the anti-diffusion correction are illustrated for 1-dimensional setting. The key idea is to sharpen the interface by applying anti-diffusion to the interface which has been smeared out due to numerical diffusion during the volume-fraction advection step. For this purpose the diffusion equation (10) is solved with a negative diffusion coefficient D. The diffusion equation (10) can be reformulated for the diffusion coefficient D set to -1, as anti-diffusion process with constant diffusion coefficient

$$\frac{\partial \alpha}{\partial \tau} = \nabla \cdot (-\nabla \alpha) \quad . \tag{11}$$

The anti-diffusion equation is ill-posed, therefore an approximate numerical solution requires regularization. A solution to an anti-diffusion equation was first proposed by Boris and Book, where the flux corrected transport (FCT) algorithm is adopted [20]. Different methods attempting to solve the anti-diffusion equation in a stabilized way by formulating a non-linear diffusion coefficient have been reported and applied in the field of image processing, e.g. "stabilized inverse diffusion equations" [21] and "forward-and-backward adaptive diffusion process" [22]. On the other hand, monotonicity preserving constraints for ensuring boundedness were studied in references [23, 24]. Imposing maximum and minimum bounds by considering the solution in the neighboring cells for ensuring boundedness on unstructured meshes was proposed by Ubbink and Issa [11]. The usage of a *minmod* function for a discrete inverse diffusion for filtering purposes in image processing was proposed by Osher and Rudin [25]. An analysis of the stabilized inverse diffusion based on a *minmod* function was carried out by Breuß et al. [26, 27]. In this paper we propose a discrete anti-diffusion equation regularized by a *minmod* function.

Below we will first illustrate the 1-dimensional discretization procedure based on a *minmod* function and then propose a modification which is suitable for a later extension to multiple dimensions and unstructured meshes.

3.1.1. Regularized anti-diffusion equation by minmod function

Considering a 1-dimensional equidistantly spaced grid, the anti-diffusion equation can be regularized and solved numerically by using a *minmod* function as given in references [26, 27] for the numerical flux calculation

$$F_{i-1/2} = \mathrm{minmod}\left(\frac{\alpha_{i+1}-\alpha_i}{\Delta x}, \frac{\alpha_i-\alpha_{i-1}}{\Delta x}, \frac{\alpha_{i-1}-\alpha_{i-2}}{\Delta x}\right) \quad , \tag{12}$$

where i indicates the cell under consideration, $F_{i-1/2}$ is the numerical flux between the cell $i-1$ and the cell i, and

$$\mathrm{minmod}\,(a,b,c) = \mathrm{sgn}\,(b)\max\left(0, \min\left(\mathrm{sgn}\,(b)\,a, |b|\,, \mathrm{sgn}\,(b)\,c\right)\right) \quad . \tag{13}$$

The calculation of $F_{i-1/2}$ requires α_{i+1}, α_i, α_{i-1} and α_{i-2}. However, the algorithm cannot be applied directly for 3-dimensional and irregular meshes as α_{i+1} and α_{i-2} are not well defined with respect to the cell face between cell i and cell $i-1$. For this reason we propose a compact re-formulation of eq. (12) as follows:

Modification 1. We decompose the numerical flux calculation by eq. (12) into the following two steps:

1. $\nabla\alpha$ at cell center is calculated based on a *minmod* function.
2. The numerical flux is calculated based on selecting $\nabla\alpha$ with minimum magnitude.

Step 1. $(\nabla\alpha)_i$ at the cell center is calculated as

$$(\nabla\alpha)_i = \operatorname{minmod}\left(\frac{\alpha_{i+1}-\alpha_i}{\Delta x}, \frac{\alpha_i-\alpha_{i-1}}{\Delta x}\right) \quad , \tag{14}$$

where

$$\operatorname{minmod}(a,b) = \begin{cases} a & \text{if } a\cdot b>0 \text{ and } |a|\le|b| \\ b & \text{if } a\cdot b>0 \text{ and } |b|\le|a| \\ 0 & \text{else} \end{cases} \quad . \tag{15}$$

Step 2. $F_{i-1/2}$ is calculated as

$$F_{i-1/2} = \begin{cases} (\nabla\alpha)_i & \text{if } |(\nabla\alpha)_i| \le \left|(\nabla\alpha)_{i-1}\right| \\ (\nabla\alpha)_{i-1} & \text{if } \left|(\nabla\alpha)_{i-1}\right| < |(\nabla\alpha)_i| \end{cases} \quad . \tag{16}$$

By combining (14) and (16) it can be shown that the resulting numerical flux function is equivalent to that of (12). Note that by (14) the calculation of $(\nabla\alpha)_i$ requires only α_{i+1}, α_i and α_{i-1}, and similarly the calculation of $(\nabla\alpha)_{i-1}$ requires only α_i, α_{i-1} and α_{i-2}.

Modification 2. We further propose an alternative to (14) and (15) for the calculation of $(\nabla\alpha)_i$

$$(\nabla\alpha)_i = \frac{\alpha_{i+1/2}-\alpha_{i-1/2}}{\Delta x} \quad , \tag{17}$$

$$\alpha_{i+1/2} = \begin{cases} \alpha_{i+1} & \text{if } a \cdot \frac{a+b}{2} > 0 \text{ and } |a| < \left|\frac{a+b}{2}\right| \\ \frac{\alpha_{i+1}+\alpha_i}{2} & \text{if } a \cdot \frac{a+b}{2} > 0 \text{ and } |a| = \left|\frac{a+b}{2}\right| \\ \alpha_i & \text{else} \end{cases} \quad , \tag{18a}$$

$$\alpha_{i-1/2} = \begin{cases} \alpha_{i-1} & \text{if } b \cdot \frac{a+b}{2} > 0 \text{ and } |b| < \left|\frac{a+b}{2}\right| \\ \frac{\alpha_i+\alpha_{i-1}}{2} & \text{if } b \cdot \frac{a+b}{2} > 0 \text{ and } |b| = \left|\frac{a+b}{2}\right| \\ \alpha_i & \text{else} \end{cases} \quad , \tag{18b}$$

where $a = \frac{\alpha_{i+1}-\alpha_i}{\Delta x}$, $b = \frac{\alpha_i-\alpha_{i-1}}{\Delta x}$ and $\frac{a+b}{2} = \frac{\alpha_{i+1}-\alpha_{i-1}}{2\Delta x}$ which is the gradient evaluated by central differencing.

By comparing (14) and (15), with (17), (18a) and (18b), it can be shown that the resulting $(\nabla\alpha)_i$ are equivalent. Note that by (18a) the evaluation of $\alpha_{i+1/2}$ requires only the directional derivative $a = \frac{\alpha_{i+1}-\alpha_i}{\Delta x}$ and the gradient evaluated by central differencing $\frac{a+b}{2} = \frac{\alpha_{i+1}-\alpha_{i-1}}{2\Delta x}$. The same holds for the calculation of $\alpha_{i-1/2}$ by (18b). $(\nabla\alpha)_i$ can then be calculated from $\alpha_{i+1/2}$ and $\alpha_{i-1/2}$ by (17).

3.1.2. Time discretization

After the numerical flux is calculated, α is forwarded in pseudo time by an explicit Euler scheme as

$$\alpha_i^{n+1} = \alpha_i^n + \frac{\left(F_{i-1/2} - F_{i+1/2}\right)}{\Delta x}\Delta\tau \quad , \tag{19}$$

where α_i^{n+1} and α_i^n are the volume fractions at the new and the old time step, respectively. $\Delta\tau$ is the pseudo-time step of the anti-diffusion process. Based on the stability analysis by Breuß [26] of the stabilized inverse diffusion, regularized by a *minmod* function, the time-step-size constraint for stable pseudo-time advancement of our anti-diffusion equation is derived accordingly as

$$\Delta\tau = \frac{(\Delta x)^2}{2\,|D|} \quad . \tag{20}$$

The effect of the anti-diffusion correction is illustrated in Fig. 1. Initially a 1-dimensional profile, increasing monotonically from $\alpha = 0$ to $\alpha = 1$ with a transition region across 6 cells, is defined, which is an analog to the numerically diffused interface of a two-phase flow. By solving the anti-diffusion equation repeatedly, the transition region becomes thinner which represents a steepened interface. As can be seen from the result, the anti-diffusion correction exhibits the desired properties which are crucial for two-phase flows with sharp interfaces: reduction of the thickness of the transition region with respect to its central position and boundedness of the volume fraction between 0 and 1.

[Figure 1 about here.]

3.1.3. Measurement of interface sharpness

After each volume-fraction advection step, the anti-diffusion correction is performed repeatedly to attain a sharp interface. In multiple dimensions and for unstructured grids a grid-independent measure of interface sharpness is required to derive a stopping criterion for the anti-diffusion iteration. For this purpose, we use the flux difference $\nabla \cdot (-\nabla\alpha_i) = \frac{\left(F_{i-1/2} - F_{i+1/2}\right)}{\Delta x}$ as a measurement of interface sharpness.

For a case- and grid-resolution-independent criterion, interface sharpness tolerances TOL_1 and TOL_2 are defined, and the term $\nabla \cdot (-\nabla\alpha_i)$ is normalized as

$$TOL_1 \leq \frac{\sum_i |\nabla \cdot (\nabla\alpha_i)|}{\sum_i |\nabla\alpha_i|^2} \quad , \tag{21}$$

$$TOL_2 \leq \frac{\max\limits_i \left(|\nabla \cdot (\nabla \alpha_i)|\right)}{\max\limits_i \left(|\nabla \alpha_i|^2\right)} \quad , \tag{22}$$

where $\sum\limits_i$ denotes the summation over all cells, $\max\limits_i$ determines the maximum value from all cells, and $\nabla \alpha_i = \frac{\alpha_{i+1} - \alpha_{i-1}}{2\Delta x}$. The evolution of TOL_1 and TOL_2 corresponding to the anti-diffusion correction in Fig. 1 is shown in Fig. 2.

[Figure 2 about here.]

3.2. Formulation of the anti-diffusion equation for multiple dimensions and unstructured meshes

To extend the idea of interface steepening by anti diffusion to multiple dimensions and unstructured meshes, and to couple the anti-diffusion algorithm with volume-fraction advection and the Navier-Stokes equations for realistic flow simulations, the diffusion coefficient is related to the numerical diffusion due to advection. A modified-differential equation analysis of the numerical diffusion induced by an upwind scheme shows that the numerical diffusion coefficient is $\frac{1}{2}\mathbf{u}\Delta x \left(1 - \frac{\mathbf{u}\Delta t}{\Delta x}\right)$ e.g. [28]. In our formulation of the anti-diffusion correction the aim is to counteract the numerical diffusion resulting from discrete advection. For this purpose the diffusion coefficient in the anti-diffusion equation is chosen to be $|\mathbf{u}|$, i.e. the diffusion coefficient D is set to $-|\mathbf{u}|$

$$\frac{\partial \alpha}{\partial \tau} = \nabla \cdot (-|\mathbf{u}| \nabla \alpha) \quad , \tag{23}$$

where $|\mathbf{u}|$ is constant in τ.

For multiple dimensions, the interface normal direction is to be taken into account so that the interface is sharpened in its normal direction. For this purpose, the anti-diffusion correction flux is projected onto the interface normal direction. Hence the diffusion equation (23) is reformulated as

$$\frac{\partial \alpha}{\partial \tau} = \nabla \cdot \left[- \left| \mathbf{u} \right| \left(\nabla \alpha \cdot \mathbf{n}_I \right) \mathbf{n}_I \right] \quad . \tag{24}$$

The interface unit normal $\mathbf{n}_I$ is calculated as

$$\mathbf{n}_I = \frac{(\nabla \alpha)^*}{|(\nabla \alpha)^*|} \quad , \tag{25}$$

where $(\nabla \alpha)^*$ is calculated by the Gauss theorem from

$$(\nabla \alpha)^* = \frac{\sum_{cf} (\alpha \mathbf{S})}{V} \quad . \tag{26}$$

Here $\sum_{cf}$ denotes the summation over all cell faces, $\mathbf{S}$ is the cell surface area vector, V is the cell volume. α is obtained by averaging the volume fractions of cells P and N (refer to Fig. 3), i.e. $\frac{\alpha_P+\alpha_N}{2}$, where α_P and α_N are the volume fractions of cell P and N respectively.

[Figure 3 about here.]

After each advection time step the anti-diffusion correction is evolved in pseudo time. Note that in order to maintain the interface location during the successive correction steps n_I is calculated at the first anti-diffusion correction step [14], i.e. $\tau = 0$. The anti-diffusion equation (24) is evaluated with constant $\mathbf{n}_I$

$$\mathbf{n}_I = \frac{(\nabla \alpha)^*_{\tau=0}}{|(\nabla \alpha)^*_{\tau=0}|} \quad . \tag{27}$$

3.3. Ensuring boundedness of the volume fraction when solving the anti-diffusion equation

Based on the regularization of the anti-diffusion equation by a *minmod* function in the 1-dimensional setting detailed in section 3.1.1, we propose a limiter based on the directional derivative to ensure boundedness of the volume fraction on unstructured meshes. The anti-diffusion algorithm involves the following steps:

1. A cell average of $\nabla\alpha$ is calculated following the Gauss theorem with a limiter based on the directional derivative.
2. The calculated cell-averaged $\nabla\alpha$ is projected onto the interface-normal direction and multiplied by the diffusion coefficient and the interface-normal vector to obtain $[-|\mathbf{u}|(\nabla\alpha\cdot\mathbf{n}_I)\,\mathbf{n}_I]$.
3. The cell-averaged divergence $\nabla\cdot[-|\mathbf{u}|(\nabla\alpha\cdot\mathbf{n}_I)\,\mathbf{n}_I]$ is calculated from the Gauss theorem.
4. An Euler explicit scheme is used for pseudo-time discretization of the anti-diffusion equation.

During pseudo-time advancement $\mathbf{n}_I$ is fixed at its initial value.

3.3.1. Calculation of $\nabla\alpha$

A limited value of the volume-fraction gradient $\nabla\alpha$ is calculated by Gauss theorem with an interpolation of the volume fraction at the cell face based on the following algorithm:

Step 1. Given cells P and N (see Fig. 3), we first calculate:

- The cell-averaged gradient $(\nabla\alpha)^*$ from equation (26) for cells P and N.
- The directional derivative $\frac{\partial\alpha}{\partial c}$ from

$$\frac{\partial\alpha}{\partial c}=\frac{(\alpha_N-\alpha_P)}{\|\mathbf{c}_N-\mathbf{c}_P\|}\quad, \tag{28}$$

where $\mathbf{c}_P$ and $\mathbf{c}_N$ are the cell-center-position vectors of cell P and N respectively.

Step 2. $(\nabla\alpha)^*_P$ is projected onto the cell-face-normal direction, leading to the term $(\nabla\alpha)^*_P\cdot\hat{\mathbf{n}}_{cf}$, where $\hat{\mathbf{n}}_{cf}$ is the cell-face unit normal of the face between the cells P and N. $(\nabla\alpha)^*_P\cdot\hat{\mathbf{n}}_{cf}$ and $\frac{\partial\alpha}{\partial c}$ are compared to select the volume fraction α' from α_P and α_N for calculating the limited gradient of volume fraction in the next step. The selection is equivalent to the step (18a) and (18b) in the 1-dimensional setting. Direction and magnitude of $(\nabla\alpha)_P^* \cdot \hat{\mathbf{n}}_{cf}$ and $\frac{\partial\alpha}{\partial c}$ are compared for choosing the volume fraction as

$$\alpha' = \begin{cases} \alpha_N & \text{if } \left[(\nabla\alpha)_P^* \cdot \hat{\mathbf{n}}_{cf}\right] \frac{\partial\alpha}{\partial c} > 0 \text{ and } \left|(\nabla\alpha)_P^* \cdot \hat{\mathbf{n}}_{cf}\right| < \left|\frac{\partial\alpha}{\partial c}\right| \\ \frac{\alpha_P+\alpha_N}{2} & \text{if } \left[(\nabla\alpha)_P^* \cdot \hat{\mathbf{n}}_{cf}\right] \frac{\partial\alpha}{\partial c} > 0 \text{ and } \left|(\nabla\alpha)_P^* \cdot \hat{\mathbf{n}}_{cf}\right| = \left|\frac{\partial\alpha}{\partial c}\right| \\ \alpha_P & \text{else} \end{cases} . \quad (29)$$

This procedure is applied to all cell faces of each cell with the respective cell neighbors N.

Step 3. The cell-averaged value of the volume-fraction gradient $(\nabla\alpha)_P$ for cell P is calculated by the Gauss theorem based on the α' selected from the *Step 2* above.

$$(\nabla\alpha)_P = \frac{\sum_{cf}(\alpha'\mathbf{S})}{V} . \quad (30)$$

This procedure is equivalent to step (17) in the 1-dimensional setting. Comparing (30) to the equation (26) it can be recognized that regularization is achieved by replacing cell-face values of α obtained from an arithmetic average by the α obtained from the above selection procedure.

3.3.2. Divergence of $[-|\mathbf{u}|(\nabla\alpha\cdot\mathbf{n}_I)\,\mathbf{n}_I]$

After obtaining $(\nabla\alpha)_P$, it is projected onto the interface-normal direction by multiplication with $\mathbf{n}_I$ which is given by equation (27). Equivalent to the calculation of the term $\nabla\cdot(-\nabla\alpha) = \frac{(F_{i-1/2}-F_{i+1/2})}{\Delta x}$ in the 1-dimensional setting, the flux at the cell face between cell P and cell N is limited by selection based on the minimum of $\|((\nabla\alpha)_P\cdot\mathbf{n}_I)\,\mathbf{n}_I\|$ and $\|((\nabla\alpha)_N\cdot\mathbf{n}_I)\,\mathbf{n}_I\|$

$$((\nabla\alpha)_P \cdot \mathbf{n}_I)\,\mathbf{n}_I = \begin{cases} ((\nabla\alpha)_P \cdot \mathbf{n}_I)\,\mathbf{n}_I & \text{if } \|\,((\nabla\alpha)_P \cdot \mathbf{n}_I)\,\mathbf{n}_I\| \leq \|\,((\nabla\alpha)_N \cdot \mathbf{n}_I)\,\mathbf{n}_I\| \\ ((\nabla\alpha)_N \cdot \mathbf{n}_I)\,\mathbf{n}_I & \text{if } \|\,((\nabla\alpha)_N \cdot \mathbf{n}_I)\,\mathbf{n}_I\| < \|\,((\nabla\alpha)_P \cdot \mathbf{n}_I)\,\mathbf{n}_I\| \end{cases} \tag{31}$$

The limited flux is further multiplied by the diffusion coefficient $-|\mathbf{u}_P|$, i.e. the cell-averaged velocity magnitude for cell P. Then the cell average of $\nabla \cdot [-|\mathbf{u}_P|\,((\nabla\alpha)_P \cdot \mathbf{n}_I)\,\mathbf{n}_I]$ is calculated by the Gauss theorem as

$$\nabla \cdot [-|\mathbf{u}_P|\,((\nabla\alpha)_P \cdot \mathbf{n}_I)\,\mathbf{n}_I] = \frac{\sum_{cf}\left([-|\mathbf{u}_P|\,((\nabla\alpha)_P \cdot \mathbf{n}_I)\,\mathbf{n}_I] \cdot \mathbf{S}\right)}{V} \quad . \tag{32}$$

3.3.3. Time-step criterion

The time derivative is discretized by an explicit Euler scheme. The volume fraction is forwarded in pseudo time by

$$\alpha^{n+1} = \alpha^n + (\nabla \cdot [-|\mathbf{u}|\,(\nabla\alpha \cdot \mathbf{n}_I)\,\mathbf{n}_I])\,\Delta\tau \quad , \tag{33}$$

where α^{n+1} and α^n are the volume fractions at the new and the old time step respectively. In the 1-dimensional setting the CFL requirement (20) for the stabilized inverse diffusion equation applies. From numerical experimentation we find that stable time integration for multiple dimensions, unstructured meshes and variable diffusion coefficient is achieved by

$$\Delta\tau = \frac{1}{4}\frac{(\Delta x)^2}{|\mathbf{u}|_{max}} \quad , \tag{34}$$

where Δx is the minimum cell width and $|\mathbf{u}|_{max}$ the maximum velocity magnitude over the entire computational domain.

3.4. Stopping criterion for the anti-diffusion correction

For defining a stopping criterion for the anti-diffusion correction formulation in multiple dimensions and unstructured meshes, the term $\nabla \cdot [-|\mathbf{u}|\left((\nabla\alpha)\cdot\mathbf{n}_I\right)\mathbf{n}_I]$ is used to measure the interface sharpness. Sharpness tolerances TOL_1 and TOL_2 are defined as

$$TOL_1 \leq \frac{\sum\limits_i |\nabla \cdot [(\nabla\alpha_i \cdot \mathbf{n}_I)\,\mathbf{n}_I]| \cdot V}{\sum\limits_i |(\nabla\alpha_i)^*|^2 \cdot V} \tag{35}$$

$$TOL_2 \leq \frac{\max\limits_i \left(|\nabla \cdot [(\nabla\alpha_i \cdot \mathbf{n}_I)\,\mathbf{n}_I]| \cdot V\right)}{\max\limits_i \left(|(\nabla\alpha_i)^*|^2 \cdot V\right)} \quad . \tag{36}$$

For demonstrating the effect of the tolerances the anti-diffusion correction is applied to a steady diffused 3-dimensional profile, Fig. 4. The corresponding evolution of TOL_1 and TOL_2 is shown in Fig. 5. For realistic flow simulations we find by numerical experimentation that a desired interface sharpness and the simulation stability can be achieved by $TOL_1 = 0.75$ and $TOL_2 = 0.75$. These interface sharpness tolerances are used in all numerical validation computations of the next section.

[Figure 4 about here.]

[Figure 5 about here.]

4. Numerical results

The anti-diffusion interface-steepening algorithm is validated with the following numerical examples. First, a 2-dimensional rising-bubble case is considered. A comparison with reference data from literature and a convergence study are carried out. Second, a 3-dimensional rising-bubble, and third a 2-dimensional and a 3-dimensional axisymmetric rising-drop on a non-Cartesian mesh are examined. In all cases for the numerical discretization of the volume-fraction-transport equation the van Leer limiter [29] is employed for calculating the flux and an Euler explicit scheme is employed for time integration. All computations are carried out with a CFL number of 0.5.

4.1. 2-dimensional rising bubble

First, the 2-dimensional rising-bubble case of Olsson and Kreiss [13] is considered. The parameters used in this numerical example are

$\rho_1 = 1,\ \ \rho_2 = 0.0013,$

$\mu_1 = 1,\ \ \mu_2 = 0.016,$

$\sigma = 7.3 \times 10^{-2}\, N/m,$

$Re = 500,\ Fr = 0.45,\ We = 0.68,$

where ρ is the density, μ is the liquid viscosity, σ is the surface tension of the liquid, and the subscripts 1 and 2 refer respectively to the water phase and the air phase. The reference parameters are $\rho_{ref} = 1.0 \times 10^3 kg/m^3$, $l_{ref} = 5.0 \times 10^{-3}\, m$ and $u_{ref} = 0.1\, m/s$. The computational domain size is $2l_{ref} \times 4l_{ref}$. The bubble is initialized at the position $(1l_{ref},\ 1l_{ref})$. Four different grid resolutions are used: $\Delta x = 2/25$, $\Delta x = 2/50$, $\Delta x = 2/100$, $\Delta x = 2/200$.

The volume-fraction contours 0.05, 0.5 and 0.95 of the bubble at $t = 0.5$ obtained by the anti-diffusion interface steepening method are shown in Fig. 6(a). The result of Olsson and Kreiss [13] is reproduced in Fig. 6(b) for comparison. Bubble-shape convergence is observed for a grid refinement from $\Delta x = 2/25$ to $\Delta x = 2/200$. The bubble shapes at lower grid resolutions are significantly more accurate than that of [13]. The bubble rising velocity is shown in Fig. 7(a), and compared with that of [13] in Fig. 7(b). The grid convergence of the rising velocity is observed to be faster than that of [13].

[Figure 6 about here.]

[Figure 7 about here.]

4.2. 3-dimensional rising bubble

Second, for validation in 3 dimensions, the case of an air bubble rising in a water-glucose solution based on the experiment carried out by Bhaga and Weber [30] is studied. The case can be characterized by the Reynolds number, the Eötvös number and the Morton number

$$Re = \frac{\rho d_B U_B}{\mu} = 2.47, \qquad E\ddot{o} = \frac{g d_e^2 \rho}{\sigma} = 116, \qquad Mo = \frac{g\mu^4}{\rho\sigma^3} = 848 \quad ,$$

where ρ is the liquid density, $d_B = 0.0261\, m$ is the bubble volume-equivalent diameter, U_B is the bubble terminal rising velocity, μ is the liquid viscosity, σ is the surface tension of the liquid and g is the gravitational acceleration.

The computational domain size is $5d_e \times 10d_e \times 5d_e$. The grid resolution is 50 x 100 x 50. A spherical bubble of $d_e = 1$ is initialized at position ($2.5d_e$, $1d_e$, $2.5d_e$). The boundary condition at the front, back, left, right and bottom domain boundaries is set as no-slip wall. Corresponding to the experimental setup of a rising bubble in a vertical tube open to the atmosphere, the top boundary is set to a free-surface boundary condition. For such a boundary condition the volume fraction can be either Neumann-type (zero gradient) or Dirichlet-type, depending on the direction of the flux [10], where the boundary condition is defined as *inlet / outlet* in the *OpenFOAM* library [15]. The pressure is adjusted by the Bernoulli equation, where the boundary condition is defined as*totalPressure* in the *OpenFOAM* library. The velocity is evaluated from the pressure and the direction of the flux, where the boundary condition is defined as *pressure inlet / outlet velocity* in the *OpenFOAM* library.

The bubble reaches a steady shape after an initial transient period. The volume-fraction contour 0.5 of the steady bubble at $t = 0.55\,s$ is shown in Fig. 8(a). The interface sharpness can be evaluated by the volume-fraction contours 0.05, 0.5 and 0.95 in Fig. 8(b). A terminal oblate-ellipsoidal-cap bubble shape is obtained, which corresponds to the experimental observation [30]. The rising velocity of the bubble is plotted in Fig. 9. The computed Reynolds number based on the terminal rising velocity from the simulation is 2.40 and compares well to the experimental Reynolds number of 2.47.

[Figure 8 about here.]

[Figure 9 about here.]

4.3. Rising drop in a periodically constricted capillary tube

Third, in order to validate the anti-diffusion correction algorithm for non-Cartesian meshes, a case of a drop rising in a periodically constricted capillary tube is considered. The case is based on the experiment carried out by Hemmat and Borhan [31] and simulated previously by Muradoglu and Kayaalp [32]. The parameters used in this numerical example are

$\rho_o = 1160\,kg/m^3$, $\rho_d = 966\,kg/m^3$,

$\mu_o = 87\,mPa\,s$, $\mu_d = 115\,mPa\,s$,

$\sigma = 0.0042\,N/m$,

where the subscripts o and d denote the ambient fluid and the drop fluid respectively. Similarly as [32], a portion of $26\,cm$ of a periodically constricted capillary tube is selected as the computational domain, which is shown in Fig. 10. The constricted capillary tube has the following geometric parameters: average radius, $R = 0.5\,cm$, wavelength of corrugations, $h = 4\,cm$, and amplitude of corrugations $A = 0.07\,cm$. The grid resolution of the computational domain is 32 x 1664. The size of the drop is measured by κ which is defined as the ratio of the equivalent spherical drop radius to R. A drop of $\kappa = 0.92$ is initialized at the height of $0.01\,cm$ along the centreline. Simulation time is non-dimensionalized by

$$t_{ref} = \frac{\mu_o}{\Delta\rho g_y R} \quad , \tag{37}$$

where t_{ref} is the reference time, $\Delta\rho = \rho_o - \rho_d$ and g_y is the gravitational acceleration.

[Figure 10 about here.]

First, a 2-dimensional planar case is simulated where the boundary condition of the top, bottom and right boundaries is no-slip wall, and at the left boundary a symmetry condition is imposed. Second, an axisymmetric 3-dimensional case is simulated.

The volume-fraction contours 0.05, 0.5 and 0.95 at different time instants are shown in Fig. 11 for the 2-dimensional planar case and the axisymmetric case. A sharp interface is obtained on the given non-Cartesian meshes for both cases. In addition it can be seen that the drop shape is periodic with respect to the periodic corrugation. This is in good agreement with the experiment [31] where it was stated that the drop deformation parameter was found to be periodic for all drop sizes without drop breakup. Note that [32] does not recover this behavior. In the 2-dimensional planar case the drop area corresponds to the drop mass, allowing to assess the discrete conservation of mass. A comparison of the drop area at different time steps with the simulation by Muradoglu and Kayaalp [32] suggests that the drop mass is better conserved by our simulations.

[Figure 11 about here.]

Further comparisons of the drop shape in the 2-dimensional planar case and the axisymmetric case, as shown in Fig. 12, reveal that the necking of the rising drop after the corrugation is more pronounced in the axisymmetric case. This agrees with the observation that periodic constrictions lead to stronger cross-section reduction in 3 dimensions than in 2 dimensions, resulting in a stronger drop deformation.

[Figure 12 about here.]

5. Concluding remarks

In this paper we have proposed an interface steepening method by an anti-diffusion correction for two-phase incompressible flows based on the VOF interface-capturing method. The method possesses the following properties: (i) no interface reconstruction is required for the volume-fraction advection, (ii) a sharp phase-interface is maintained throughout the simulation, and (iii) a desired interface sharpness can be attained based on a case- and grid-resolution -independent interface sharpness measurement.

First, in a 1-dimensional setting an anti-diffusion equation is formulated, and the equation is solved after each volume-fraction advection. A *minmod* function is employed to regularize the anti-diffusion equation for a numerical solution. Modifications to the *minmod* function, which allow for an extension to multiple dimension and unstructured meshes, are presented. 1-dimensional results show that the interface can be steepened and the boundedness of the volume-fraction is preserved. A suitable interface sharpness measurement is developed that does not require the evaluation of additional terms as it is based on the flux difference directly.

The anti-diffusion method is extended to multiple dimensions and unstructured meshes, and coupled with the volume-fraction advection and the Navier-Stokes equation for realistic flow simulations. The anti-diffusion equation is reformulated by taking into account the interface normal direction and by adopting the velocity magnitude as the diffusion coefficient, following modified-differential equation analysis of the numerical diffusion due to advection. A limiter based on the directional derivative, which follows the 1-dimensional modified *minmod* function, is proposed and allows for stable solution of the anti-diffusion equation. The anti-diffusion correction can be carried out repeatedly to attain a desired interface sharpness. A stopping criterion for the anti-diffusion iteration, which is based on the interface sharpness measurement, is developed.

Validation computations are performed for 2- and 3- dimensional rising-bubble and rising-drop configurations, and for Cartesian and non-Cartesian meshes. The results agree well with experiments and show the advantages of the current method in comparison with previous simulations by other methods. In particular, the method is more accurate at low grid resolutions and the grid convergence is faster as compared, e.g., to reference [13]. The simulation of a drop rising in a periodically constricted capillary tube by our method reproduces the experimental observation of periodic drop-deformation [31], which suggests that the current method is a significant improvement as compared to reference [32].

Though originally being proposed for solving the anti-diffusion equation, two aspects of the present method may also be applied to other computational modeling problems. First, as the proposed modification of the *minmod* function can be employed as a general slope limiter, it may also be applied to more general equations on unstructured meshes than has been done in this paper. Second, as the proposed interface-sharpness measurement gives a general assessment of a VOF interface representation, which is independent of the specific interface-steeping method, it may also be used within other methods such as the artificial-compression steepening [13].

References

[1] S. O. Unverdi, G. Tryggvason, A front-tracking method for viscous, incompressible, multi-fluid flows, Journal of Computational Physics 100 (1) (1992) 25-37.

[2] G. Tryggvason, B. Bunner, A. Esmaeeli, D. Juric, N. Al-Rawahi, W. Tauber, J. Han, S. Nas, Y. J. Jan, A front-tracking method for the computations of multiphase flow, Journal of Computational Physics 169 (2) (2001) 708-759.

[3] D. J. Torres, J. U. Brackbill, The point-set method: Front-tracking without connectivity, Journal of Computational Physics 165 (2) (2000) 620-644.

[4] R. Scardovelli, S. Zaleski, Direct numerical simulation of free-surface and interfacial flow, Annual Review of Fluid Mechanics 31 (1999) 567-603.

[5] S. Osher, R. P. Fedkiw, Level set methods: An overview and some recent results, Journal of Computational Physics 169 (2) (2001) 463-502.

[6] J. A. Sethian, P. Smereka, Level set methods for fluid interfaces, Annual Review of Fluid Mechanics 35 (2003) 341-372.

[7] W. J. Rider, D. B. Kothe, Reconstructing volume tracking, Journal of Computational Physics 141 (2) (1998) 112-152.

[8] W. Noh, P. Woodward, Lecture Notes in Physics, Springer Berlin, 1976.

[9] C. W. Hirt, B. D. Nichols, Volume of fluid (VOF) method for the dynamics of free boundaries, Journal of Computational Physics 39 (1) (1981) 201-225.

[10] H. Rusche, Computational fluid dynamics of dispersed two-phase flows at high phase fractions, Ph.D. thesis, Imperial College of Science, Technology & Medicine (2002).

[11] O. Ubbink, R. I. Issa, A method for capturing sharp fluid interfaces on arbitrary meshes, Journal of Computational Physics 153 (1) (1999) 26-50.

[12] Z. Xu, C.-W. Shu, Anti-diffusive flux corrections for high order finite difference WENO schemes, Journal of Computational Physics 205 (2) (2005) 458-485.

[13] E. Olsson, G. Kreiss, A conservative level set method for two phase flow, Journal of Computational Physics 210 (1) (2005) 225-246.

[14] E. Olsson, G. Kreiss, S. Zahedi, A conservative level set method for two phase flow II, Journal of Computational Physics 225 (1) (2007) 785-807.

[15] Openfoam, http://www.opencfd.co.uk/openfoam/, version 1.5.

[16] J. U. Brackbill, D. B. Kothe, C. Zemach, A continuum method for modeling surface tension, Journal of Computational Physics 100 (2) (1992) 335-354.

[17] H. Jasak, H. G. Weller, A. D. Gosman, High resolution NVD differencing scheme for arbitrarily unstructured meshes, International Journal for Numerical Methods in Fluids 31 (2) (1999) 431-449.

[18] R. I. Issa, Solution of the implicitly discretised fluid flow equations by operator-splitting, Journal of Computational Physics 62 (1) (1986) 40-65.

[19] O. Ubbink, Numerical prediction of two fluid systems with sharp interfaces, Ph.D. thesis, Imperial College of Science, Technology & Medicine (1997).

[20] J. P. Boris, D. L. Book, Flux-corrected transport. I. SHASTA, a fluid transport algorithm that works, Journal of Computational Physics 11 (1) (1973) 38-69.

[21] I. Pollak, A. S. Willsky, H. Krim, Image segmentation and edge enhancement with stabilized inverse diffusion equations, IEEE Transactions on Image Processing 9 (2) (2000) 256-266.

[22] G. Gilboa, N. Sochen, Y. Y. Zeevi, Forward-and-backward diffusion processes for adaptive image enhancement and denoising, IEEE Transactions on Image Processing 11 (7) (2002) 689-703.

[23] D. S. Balsara, C.-W. Shu, Monotonicity preserving weighted essentially non-oscillatory schemes with increasingly high order of accuracy, Journal of Computational Physics 160 (2) (2000) 405-452.

[24] W. J. Rider, L. G. Margolin, Simple modifications of monotonicity-preserving limiter, Journal of Computational Physics 174 (1) (2001) 473-488.

[25] S. Osher, L. I. Rudin, Shocks and other nonlinear filtering applied to image processing, Vol. 1567, SPIE, 1991, pp. 414-431.

[26] M. Breuß, T. Brox, T. Sonar, J. Weickert, Stabilized nonlinear inverse diffusion for approximating hyperbolic PDEs, Scale Space and PDE Methods in Computer Vision, Proceedings 3459 (2005) 536-547.

[27] M. Breuß, M. Welk, Staircasing in semidiscrete stabilized inverse linear diffusion algorithms, Journal of Computational and Applied Mathematics 206 (1) (2007) 520-533.

[28] R. J. Leveque, Finite Volume Methods for Hyperbolic Problems, Cambridge University Press, 2002.

[29] B. van Leer, Towards the ultimate conservative difference scheme. II. monotonicity and conservation combined in a second-order scheme, Journal of Computational Physics 14 (4) (1974) 361-370.

[30] D. Bhaga, M. E. Weber, Bubbles in viscous-liquidsshapes, wakes and velocities, Journal of Fluid Mechanics 105 (Apr) (1981) 61-85.

[31] M. Hemmat, A. Borhan, Buoyancy-driven motion of drops and bubbles in a periodically constricted capillary, Chemical Engineering Communications 150 (1996) 363-384.

[32] M. Muradoglu, A. D. Kayaalp, An auxiliary grid method for computations of multiphase flows in complex geometries, Journal of Computational Physics 214 (2) (2006) 858-877.

List of Figures

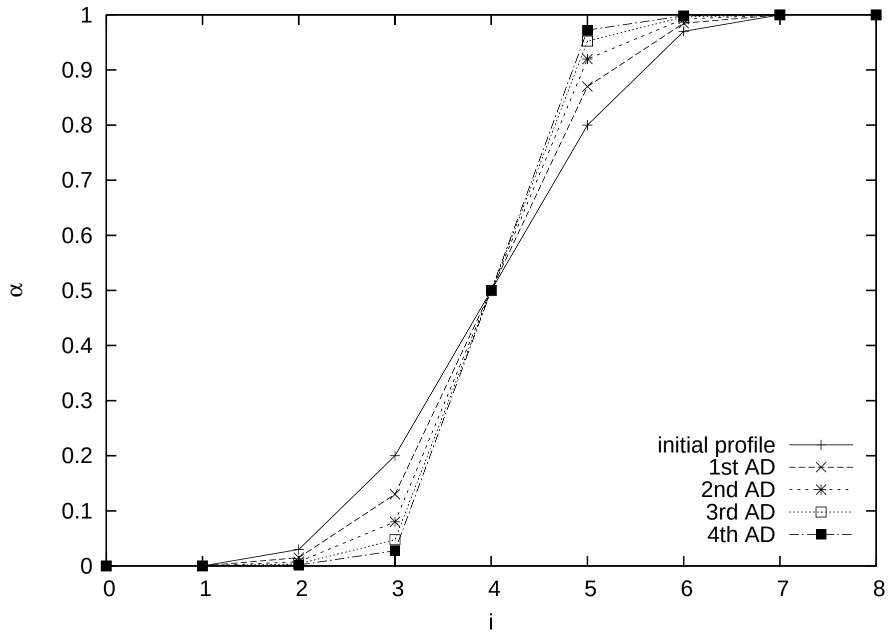

Figure 1: 1-dimensional profile of volume fraction α from value 0 to 1. i denotes the cell index. 1st AD denotes the profile after the first anti-diffusion correction.

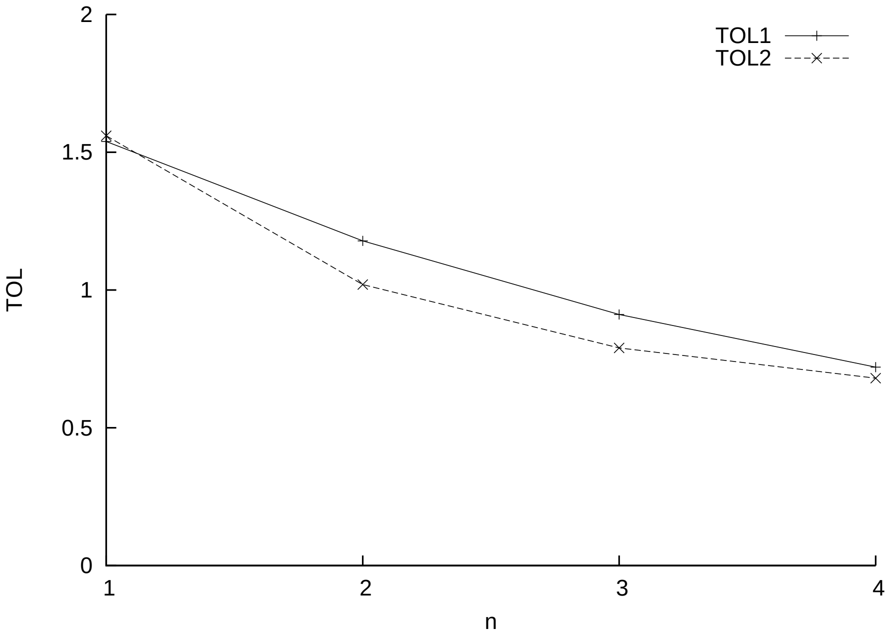

Figure 2: Evolution of TOL_1 and TOL_2 corresponding to the anti-diffusion correction in Fig. 1. n denotes the number of anti-diffusion correction.

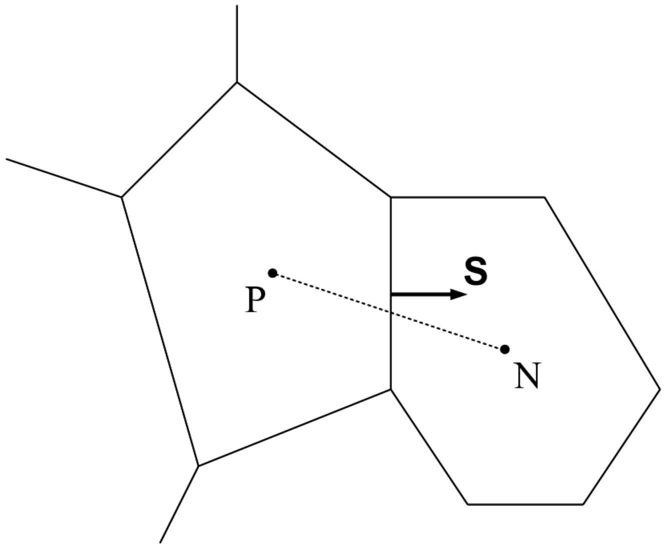

Figure 3: The cell arrangement in unstructured meshes.

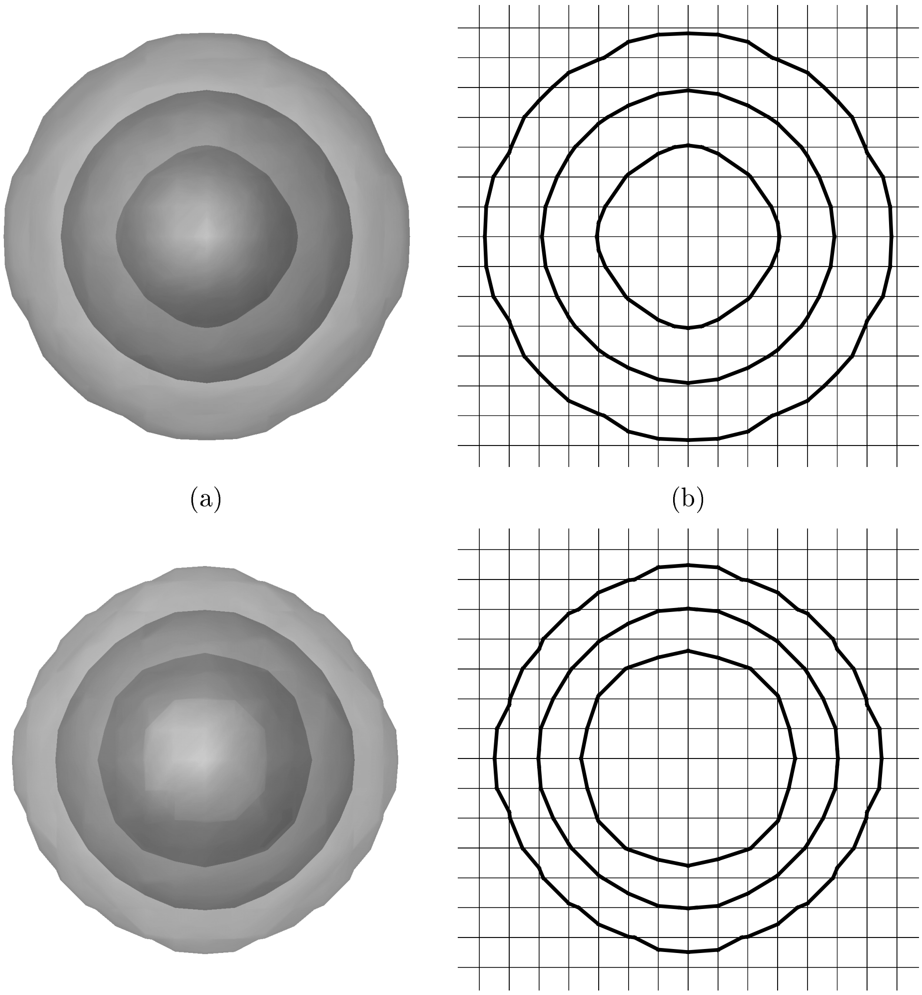

(a) (b) (c) (d)

Figure 4: Volume-fraction contours 0.05, 0.5 and 0.95 of a 3-dimensional diffused profile. (a) Initial profile (3-dimensional view). (b) Initial profile (sectional view). (c) Profile after 4 anti-diffusion corrections (3-dimensional view). (d) Profile after 4 anti-diffusion corrections (sectional view).

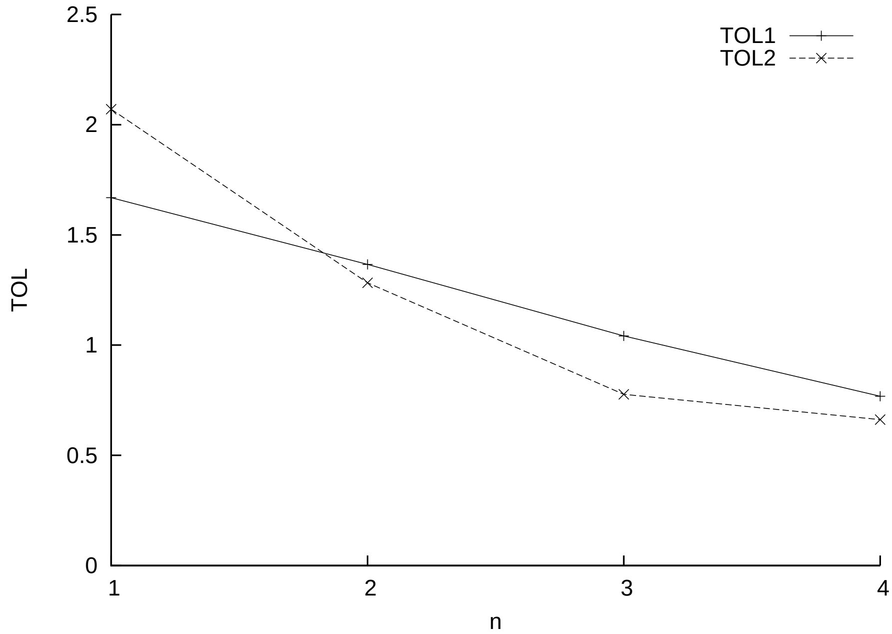

Figure 5: Evolution of TOL_1 and TOL_2 corresponding to the anti-diffusion correction in Fig. 4. n denotes the number of anti-diffusion correction.

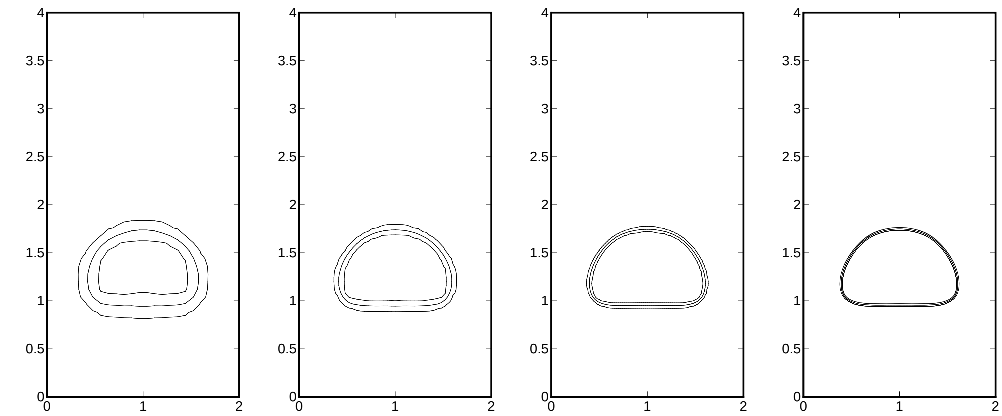

(a)

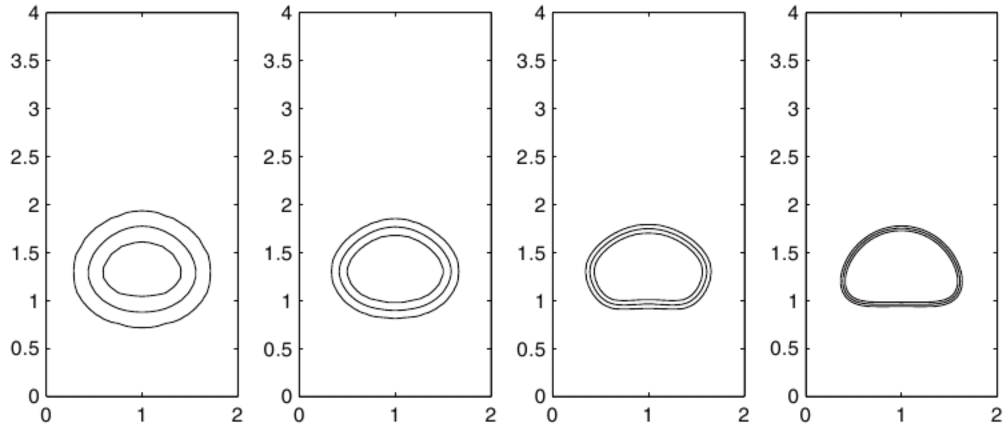

(b)

Figure 6: The volume-fraction contours 0.05, 0.5, 0.95 of the bubble at$t = 0.5$ in four different grid resolutions. From left to right: $\Delta x = 2/25$, $\Delta x = 2/50$, $\Delta x = 2/100$,$\Delta x = 2/200$. (a) Result by anti-diffusion interface sharpening. (b) Result of Olsson and Kreiss [13], reproduced with permission.

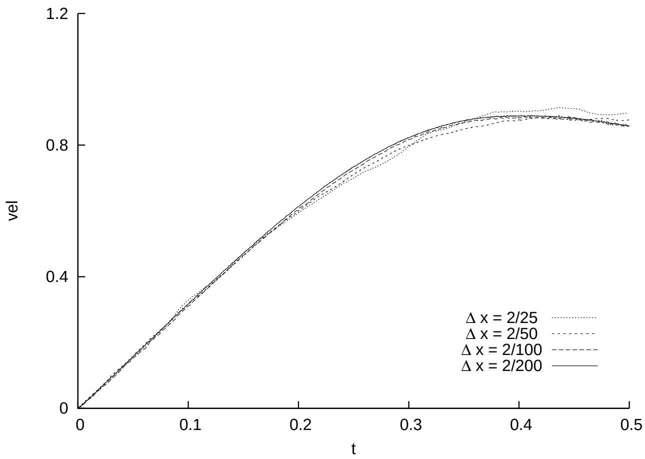

(a)

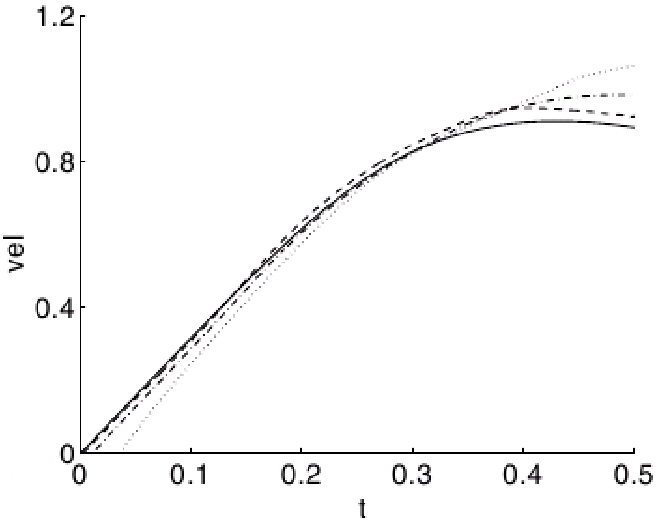

(b)

Figure 7: The rising velocity of the bubble in four different grid resolutions. (a) Result by anti-diffusion interface sharpening. (b) Result of Olsson and Kreiss [13], reproduced with permission. Dotted line: 25×50; dashed-dotted line: 50×100; dashed line: 100×200; solid line: 200×400.

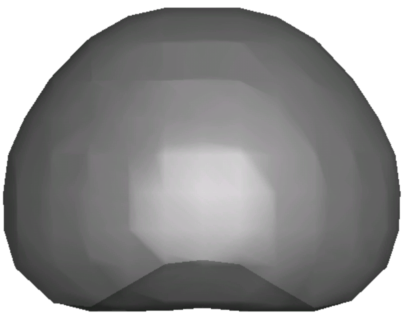

(a)

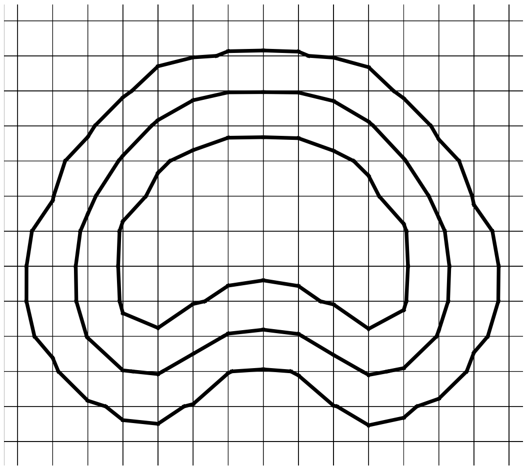

(b)

Figure 8: (a) 3-dimensional view of volume-fraction contour 0.5 of the bubble at steady state at $t = 0.55s$. (b) Sectional view of volume-fraction contours 0.05, 0.5 and 0.95 of the bubble at steady state at $t = 0.55s$.

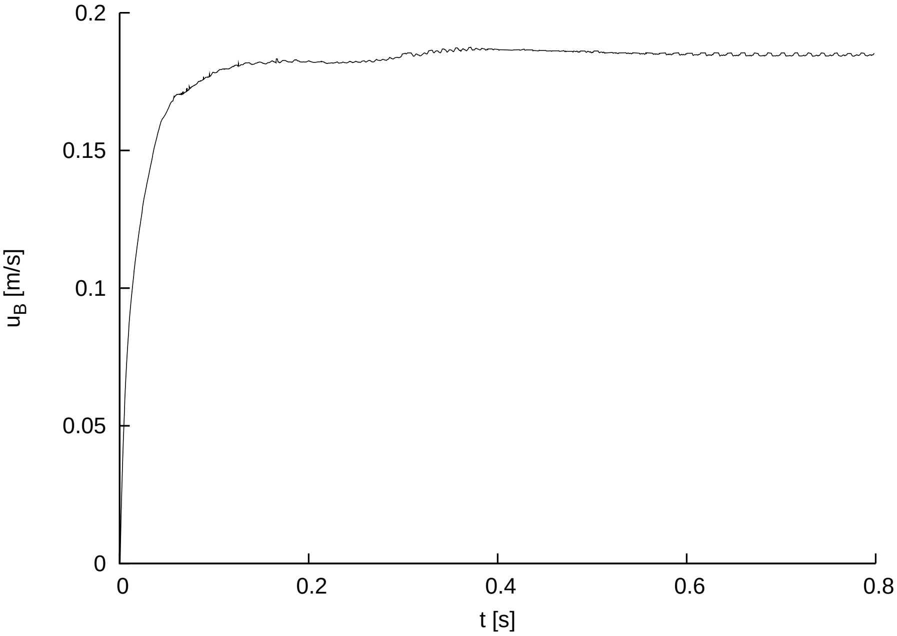

Figure 9: The rising velocity u_B of the bubble in the 3-dimensional rising-bubble case.

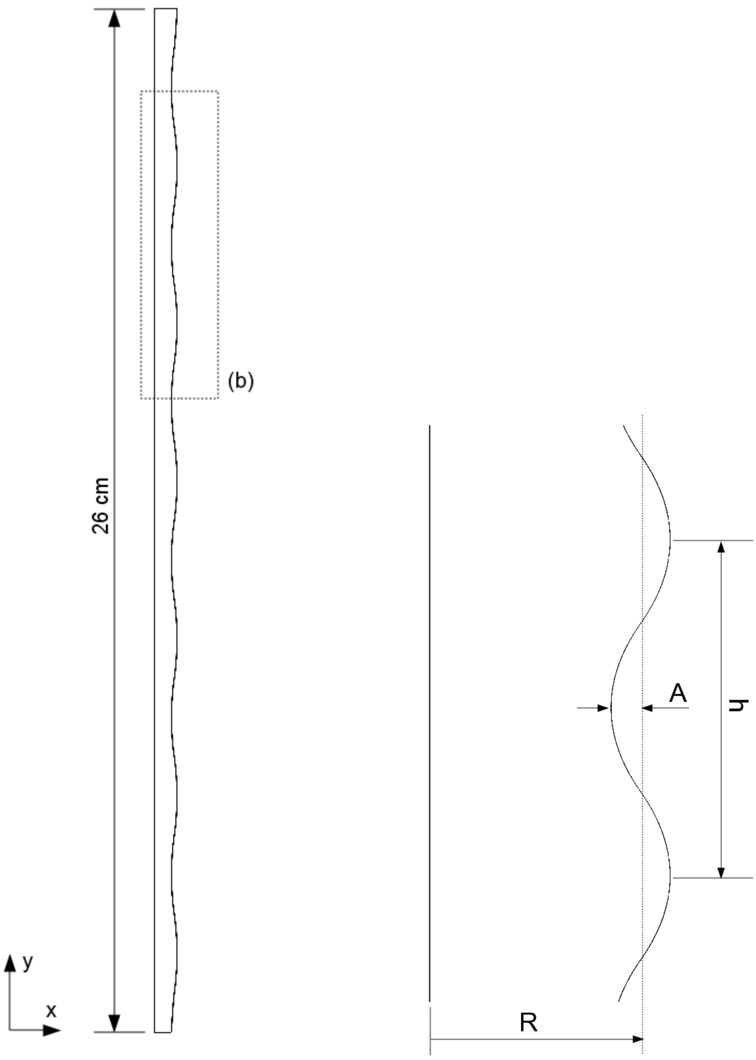

(a) (b)

Figure 10: The computational domain for case of 2-dimensional rising drop in a periodically constricted capillary tube. (a) Full domain. (b) Plan view showing dimensional details (not to scale).

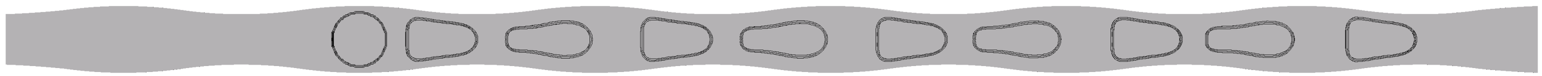

(a)

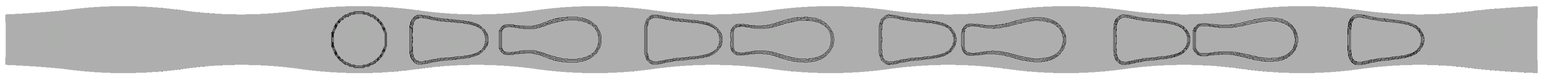

(b)

Figure 11: The volume-fraction contours 0.05, 0.5 and 0.95 of the rising drop. (a) Plots for*2-dimensional planar* simulation from $t = 0$ to $t = 3937.5$ at time interval of 437.5. (b) Plots for *axisymmetric 3-dimensional* simulation from $t = 0$ to $t = 4823.1$ at time interval of 535.9.

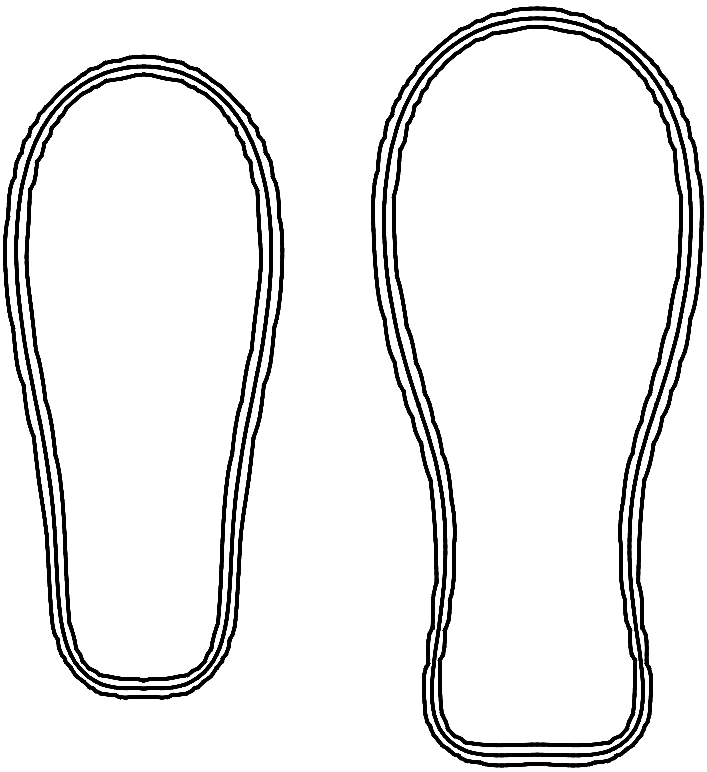

(a) (b)

Figure 12: The volume-fraction contours 0.05, 0.5 and 0.95 of the rising drop. (a) Plot at $t = 1750$ for the *2-dimensional planar* simulation. (b) Plot at $t = 2143.6s$ for the *axisymmetric 3-dimensional* simulation.